GEOPHYSICS, VOL. 73, NO. 1 (JANUARY-FEBRUARY 2008); P. S17–S26, 17 FIGS.
10.1190/1.2821193

Wave-equation angle-domain common-image gathers for converted waves

Daniel A. Rosales[1], Sergey Fomel[2], Biondo L. Biondi[1], and Paul C. Sava[3]

ABSTRACT

Wavefield-extrapolation methods can produce angle-domain common-image gathers (ADCIGs). To obtain ADCIGs for converted-wave seismic data, information about the image dip and the P-to-S velocity ratio must be included in the computation of angle gathers. These ADCIGs are a function of the half-aperture angle, i.e., the average between the incidence angle and the reflection angle. We have developed a method that exploits the robustness of computing 2D isotropic single-mode ADCIGs and incorporates both the converted-wave velocity ratio γ and the local image dip field. It also maps the final converted-wave ADCIGs into two ADCIGs, one a function of the P-incidence angle and the other a function of the S-reflection angle. Results with both synthetic and real data show the practical application for converted-wave ADCIGs. The proposed approach is valid in any situation as long as the migration algorithm is based on wavefield downward continuation and the final prestack image is a function of the horizontal subsurface offset.

INTRODUCTION

The imaging operator, prestack wavefield downward-continuation depth migration, transforms the data — which are in data-midpoint position, data-offset, and time coordinates (m_D, h_D, t) — into an image that is in image-midpoint location, offset, and depth coordinates (m_ξ, h, z_ξ). This image provides information about the accuracy of the velocity model in the redundancy of the prestack seismic image, i.e., nonzero-offset images. The subsets of this image for a fixed image point m_ξ with coordinates (z_ξ, h) are known as common-image gathers (CIGs). If the CIGs are a function of (z_ξ, h), the gathers also are referred to as offset-domain common-image gathers (ODCIGs). The CIGs also can be expressed in terms of the opening angle θ by transforming the offset axis h into θ to obtain a CIG with coordinates (z_ξ, θ); these gathers are known as angle-domain common-image gathers (ADCIGs) (de Bruin et al., 1990; Prucha et al., 1999). Rickett and Sava (2002) describe both ODCIGs and ADCIGs for wave-equation shot-profile migration.

Two-dimensional ODCIGs can be transformed into the angle domain by following a Fourier domain approach as presented by Sava and Fomel (2003). Furthermore, Fomel (2004) presents the accurate equations for 3D ADCIGs. ADCIGs are important in velocity analysis because the residual moveout present in these angle gathers is related to velocity perturbations and can be used through wavefield downward-continuation imaging (Biondi and Symes, 2004).

There are two kinds of ODCIGs: those produced by Kirchhoff migration and those produced by wave-equation migration, which have a conceptual difference in the offset dimension. For Kirchhoff ODCIGs, the offset dimension is a data parameter ($h = h_D$) and involves the concept of flat gathers. For wave-equation ODCIGs, the offset dimension is a model parameter ($h = h_\xi$) and involves the concept of focused events. In this paper, we refer to these gathers as subsurface offset-domain common-image gathers (SODCIGs) to differentiate them from the Kirchhoff ODCIGs. An event in an angle section uniquely determines a ray couple, which in turn uniquely locates the reflector. Therefore, the image representation in the angle domain does not have artifacts attributable to multipathing (Stolk and Symes, 2002). Unlike ODCIGs, ADCIGs produced with Kirchhoff and wave-equation methods have similar characteristics because the ADCIGs describe reflectivity as a function of the reflection angle.

We present a methodology to transform SODCIGs that are produced with wavefield downward-continuation migration into ADCIGs for converted-wave seismic data (PS-ADCIGs). It also presents the option to transform the PS-ADCIGs into two ADCIGs: one a function of the P-wave incidence angle and one a function of the S-wave reflection angle. We refer to these as P-ADCIGs and S-ADCIGs, respectively.

Throughout this process, the ratio between the different velocities plays an important role in the transformation. We show the equations for this mapping and show results on two simple synthetic data sets

Manuscript received by the Editor 1 March 2007; revised manuscript received 11 July 2007; published online 28 December 2007.
[1]Stanford University, Stanford Exploration Project, Department of Geophysics, Stanford, California, U.S.A. E-mail: drosales@earthworks2020.com; biondo@sep.stanford.edu.
[2]University of Texas at Austin, Bureau of Economic Geology, Austin, Texas, U.S.A. E-mail: sergey.fomel@beg.utexas.edu.
[3]Colorado School of Mines, Center for Wave Phenomena, Department of Geophysics, Golden, Colorado, U.S.A.
© 2008 Society of Exploration Geophysicists. All rights reserved.

that do not present multipathing problems. We also show results on a 2D real data set from the Mahogany field in the Gulf of Mexico. For this exercise, a comparison between the ADCIGs for the converted-wave image and for the compressional-wave image yields information that can improve the PS image.

TRANSFORMATION TO THE ANGLE DOMAIN

The transformation of PS-SODCIGs to the angle domain follows a similar approach to the 2D isotropic single-mode (PP) method (Sava and Fomel, 2003). Figure 1 describes the angles we use in this section. For the converted-mode case, we define the following angles:

$$\theta \equiv \frac{\phi + \sigma}{2},$$

$$\alpha \equiv \frac{2\alpha_x + \phi - \sigma}{2}. \tag{1}$$

where the angles ϕ, σ, and α_x represent the incident, reflected, and geologic dip angles, respectively. This definition is consistent with the single-mode case. Note that for the single-mode case, ϕ and σ are the same; therefore, θ represents the reflection angle and α represents the geologic dip (Sava and Fomel, 2003; Biondi and Symes, 2004). For the converted-mode case, ϕ and σ are not the same; hence, θ is the half-aperture angle and angle α is the pseudogeologic dip.

Throughout this paper, we present a relationship between the known quantities from our image, $I(m_\xi, z_\xi, h_\xi)$ and θ. Appendix A presents the full derivation of this relationship. Here, we present only the final result, its explanation, and its implications. The final relationship to obtain converted-mode ADCIGs is as follows (Appendix A):

$$\tan\theta = \frac{4\gamma(m_\xi,z_\xi)\tan\theta_0 + \delta[\gamma^2(m_\xi,z_\xi) - 1](\tan^2\theta_0 + 1)}{\tan^2\theta_0[\gamma(m_\xi,z_\xi) - 1]^2 + [\gamma(m_\xi,z_\xi) + 1]^2}, \tag{2}$$

where

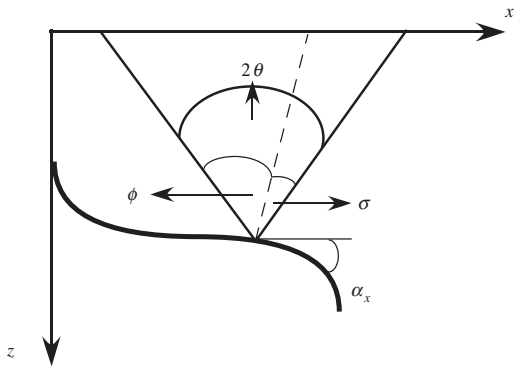


Figure 1. Definition of angles for the converted-mode reflection experiment. Angles θ, ϕ, σ, and α_x represent the half-aperture, incident, reflection, and geologic dip angles, respectively.

$$\tan\theta_0 = -\frac{\partial z_\xi}{\partial h_\xi},$$

$$\delta = -\frac{\partial z_\xi}{\partial m_\xi}.$$

Equation 2 consists of three main components: the P-to-S velocity ratio $\gamma(m_\xi, z_\xi)$; the *pseudo-opening* angle θ_0, which is the angle obtained throughout the conventional method to transform SODCIGs into isotropic ADCIGs as described by Sava and Fomel (2003); and the field of local image dips δ.

Equation 2 describes the transformation from the subsurface-offset domain into the angle domain for converted-wave data. This equation is valid under the assumption of constant velocity; however, it remains valid in a differential sense in an arbitrary velocity medium by considering that h_ξ is the subsurface half-offset (Sava and Fomel, 2003). Therefore, the limitation of constant velocity applies in the neighborhood of the image. For $\gamma(m_\xi, z_\xi)$, every point of the image is related to a point on the velocity model that has the same image coordinates. For the nonphysical case of $v_p = v_s$, i.e., no converted waves, $\gamma(m_\xi, z_\xi) = 1$, and angles θ_0 and θ are the same. Appendix B presents a derivation of equation 2 that follows a Kirchhoff approach, whereas Appendix C presents an alternative approach.

Mapping of PS-ADCIGs

Following definition 1 and after explicitly computing the half-aperture angle using equation 2, we have almost all of the tools for computing the P-incidence angle ϕ and the S-reflection angle σ. Snell's law and the P-to-S velocity ratio are the final two components needed. The result of this process will be the mapping the PS-ADCIGs that are functions of the half-aperture angle into two angle gathers. The first one, P-ADCIG, is a function of the P-incidence angle. The second one, S-ADCIG, is a function of the S-reflection angle. After basic algebraic and trigonometric manipulations, the final two expressions for this mapping are (Appendix D):

$$\tan\phi = \frac{\gamma\sin 2\theta}{1 + \gamma\cos 2\theta}, \tag{3}$$

and

$$\tan\sigma = \frac{\sin 2\theta}{\gamma + \cos 2\theta}. \tag{4}$$

Expressions 3 and 4 clearly show a nonlinear relation between the half-aperture angle and both the incident and reflection angles. The main purpose of this set of equations is to observe and analyze the converted-wave angle gathers in domains corresponding to the incidence and reflection angles. The analysis of these angle gathers might help to obtain residual moveout equations for both the P-velocity and the S-velocity and, therefore, individual updates for each of the velocity models.

METHODOLOGY

We present a method to implement equations 2–4. First, we describe the method; then, we illustrate it with a simple synthetic example. Throughout this section, we refer to two different methods: the conventional one and the proposed one. The conventional meth-

od transforms SODCIGs into ADCIGs, as in the single-mode case (Sava and Fomel, 2003). Figure 2 shows the basic steps to implement and obtain the true ADCIGs for converted-wave data (PS-ADCIGs). First, we use the final image $I(m_\xi, z_\xi, h_\xi)$ to obtain two main pieces of information: The pseudo-opening angle gathers tan θ_0, using, for example, the Fourier-domain approach (Sava and Fomel, 2003), and the estimated image dip δ, using plane-wave destructors (Fomel, 2002).Then we combine tan θ_0 and δ with the $\gamma(m_\xi, z_\xi)$ field, using equation 2 to obtain the proposed PS-ADCIGs. Finally, we map these PS-ADCIGs into the P-ADCIGs and the S-ADCIGs using equations 3 and 4, respectively.

Figure 3 shows a simple synthetic example that illustrates the flow in Figure 2. The synthetic data set consists of a single shot experiment over a 30° dipping layer. Figure 3a shows the shot gather; observe that the top of the hyperbola is not at zero offset because of the reflector dip and that the polarity flip does not happen at the top of the hyperbola. Figure 3b shows the image of the single shot gather, which represents $I(m_\xi, z_\xi, h_\xi)$ in Figure 2. The solid line in Figure 3b represents the location for the CIG in study. For this experiment, the shot location is at 500 m, with the CIG at 1000 m, and the geometry given for the reflector, the half-aperture angle, should be 35°. This corresponds to a value of tan $\theta \approx 0.7$, which is represented by a solid line on the CIGs in Figure 3c and d.

The ADCIG in Figure 3c was obtained with the conventional method. Observe that the angle obtained is not the correct one. This ADCIG represents the tangent of the pseudo-opening angle tan θ_0 of Figure 2. Combining the ADCIG in Figure 3c with the dip information δ and the $\gamma(m_\xi, z_\xi)$ field results in the proposed PS-ADCIG. Figure 3d presents the result of this process. Notice the angle in the true PS-ADCIG coincides with the correct angle.

The last step in the Figure 2 flow chart corresponds to mapping the proposed PS-ADCIG into a P-ADCIG and an S-ADCIG, corresponding to the P-incidence ϕ and S-reflection σ angles, respectively. Figure 4 shows the result of this transformation. Figure 4a is the same image for the single shot gather on a 30° dipping layer. Figure 4b is the proposed PS-ADCIG, which is taken at the location marked in the image. Figure 4c and d presents the PS-ADCIG mapped into the P-ADCIG and the S-ADCIG, respectively. The angle gathers are obtained using equations 3 and 4, respectively.

In this experiment, the computed value for the P-incidence angle is 47°, which corresponds to tan $\phi \approx 1.09$. The computed value for the S-reflection angle is 22°, which corresponds to tan $\sigma \approx 0.4$. Both of these values are represented by the vertical lines in each of the three ADCIGs in Figure 4.

Synthetic data test

The second synthetic example illustrates the importance of computing adequate PS-ADCIGs. For this purpose, we use the polarity-flip characteristic of converted-wave data. This polarity change is an intrinsic property of the shear-wave displacement (Danbom and Domenico, 1988). In a constant-velocity medium, the vector displacement field produces opposite movements in the receivers at either side of the intersection of the normal ray with the surface. In true PS-ADCIGs, the correct representation of the polarity flip should happen at zero angle because the zero angle represents normal incidence and there is no conversion from P to

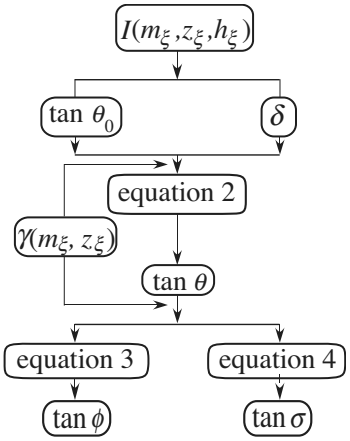


Figure 2. Flow chart for transforming the subsurface-offset CIGs into the angle domain and for mapping into P-ADCIGs and S-ADCIGs.

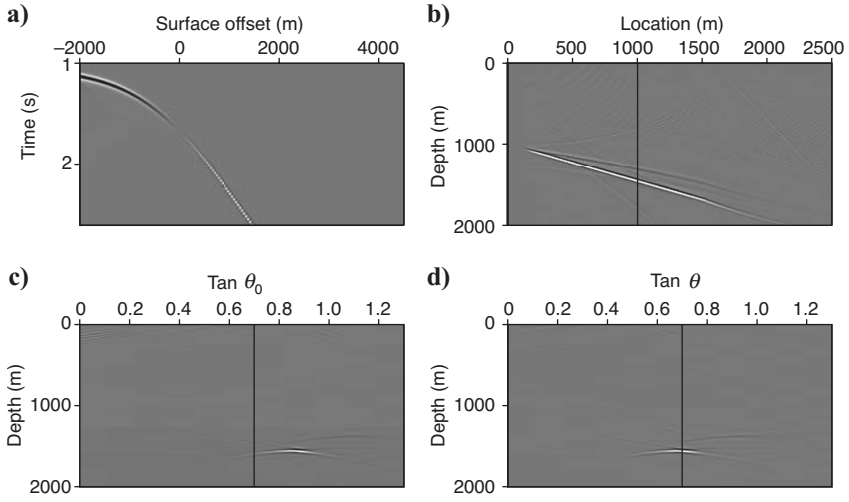


Figure 3. Synthetic example that illustrates the method in Figure 2. (a) A single shot gather for a 30° dipping layer event. (b) The image of that single shot gather. (c) The pseudo-opening angle, tan θ_0. (d) The true PS-ADCIG.

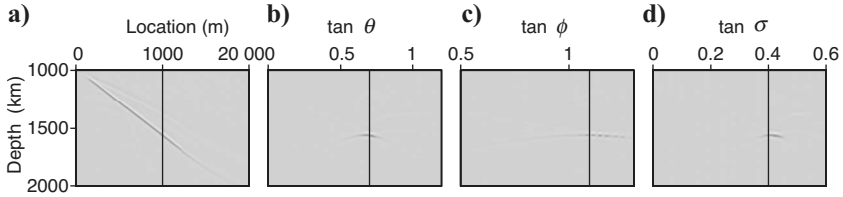


Figure 4. Synthetic example that illustrates the last step of the method on Figure 2. (a) Image of a single shot gather on a 30° dipping layer. (b) The true PS-ADCIG taken at 1000 m. (c) P-ADCIG. (d) S-ADCIG.

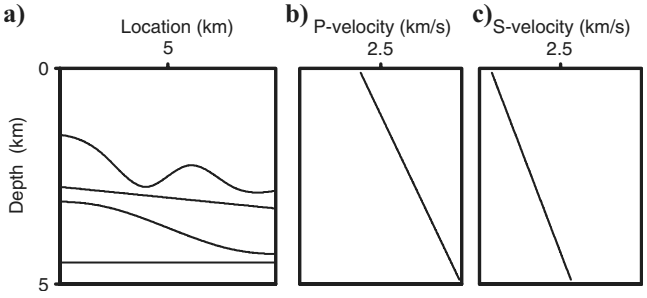


Figure 5. Synthetic model (a) layer distribution, (b) P-velocity model, and (c) S-velocity model.

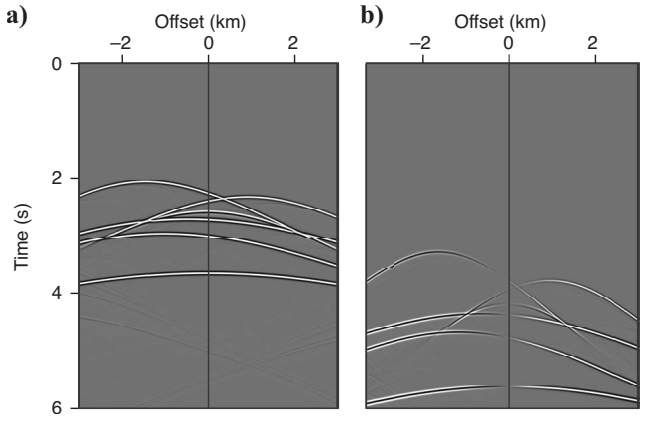


Figure 6. Single common-shot gather for the synthetic model in Figure 5. (a) PP gather. (b) PS gather.

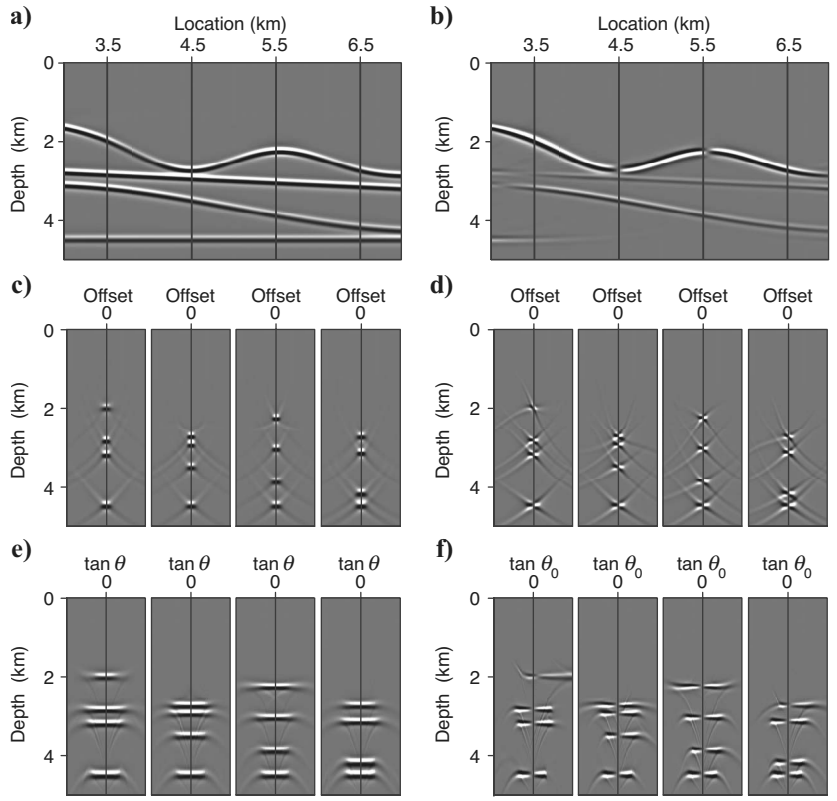


Figure 7. Migration result for the synthetic example. Views in the left column are the result for the PP section. Views in the right column are the result for the PS section. (a, b) The image at zero subsurface offset. (c, d) The SODCIGs taken at the position marked on the image. (e, f) The ADCIGs.

S energy at normal incidence. The normal incidence location is the point in the image space that distinguishes opposite particle motion; hence, the separation between positive and negative polarities.

The model depicted in Figure 5 (Baina et al., 2002) includes both gentle and steep dips (Figure 5a). The P-velocity (Figure 5b) and S-velocity (Figure 5c) models consist of a vertical gradient for a nonconstant γ value. The data set was created with an analytical Kirchhoff modeling scheme. The synthetic data set consists of 200 shots with a shot spacing of 50 m and 400 receivers with a receiver spacing of 25 m. Figure 6 shows a single common-shot gather for this data set. Figure 6a exhibits the PP component, and Figure 6b shows the PS component.

We migrated the synthetic data using a wave-equation shot-profile migration scheme. Figure 7 shows the final migration result, together with four selected CIGs. Represented are the zero subsurface-offset section for the PP (Figure 7a) and the PS (Figure 7b) migrations. Four vertical lines at locations 3.5, 4.5, 5.5, and 6.5 km are superimposed into both migrated sections. These lines represent the locations for the four CIGs beneath each migration result. Figure 7c and d represents the SODCIGs taken at the positions indicated by the vertical lines on the migration result. Figure 7e and f shows the ADCIGs; the PP-ADCIGs (Figure 7e) and PS-ADCIGs (Figure 7f) were obtained with the conventional method.

The result for the PP image is accurate; all of the energy is focused at zero subsurface offset, and the angle gathers are completely flat. This is the expected result because we performed the migration with the correct velocity model. The PS results are different. Adequate handling of amplitudes requires a true-amplitude one-way wave-equation operator (Zhang et al., 2003, 2007). We present relative results based only on positive and negative values of the amplitudes after migration to locate the polarity flip point in the image space.

First, the migration section at zero subsurface offset has positive and negative amplitudes along the first reflection. The flat reflector has vanished because there is no conversion from P to S energy at normal incidence. The SODCIGs are focused at zero, and the polarity changes across the zero value. The PS-ADCIGs are obtained with the conventional method; therefore, they represent only the pseudo-opening angle. We follow the method previously described and combine the PS-ADCIGs with the image dip information (Figure 8) to obtain the proposed PS-ADCIGs.

Figure 9 shows the proposed PS-ADCIGs. Figure 9a and c presents the same PS result as in Figure 7b and f. Figure 9a is the image at zero subsurface offset. Figure 9c shows the PS-ADCIGs. Figure 9b and d presents the final PS result. Figure 9b is the result of stacking in the angle domain using the proposed PS-ADCIGs after correcting the polarity flip (Rosales and Rickett, 2001). Figure 9d shows the proposed PS-ADCIGs, which are taken at the locations marked by the vertical lines in the final image.

In Figure 9, the areas marked with an oval in both the conventional PS-ADCIGs and the proposed PS-ADCIGs are taken at different reflectors for different dip values. The CIG at 3.5 km shows the most significant change; the polarity

flip is completely corrected at zero angle, and there is larger angle coverage because equation 2 stretches the events horizontally for an accurate representation of the half-aperture angle. Although the changes with respect to the polarity flip in the other CIGs are not that obvious, the polarity flip is now located at zero angle. Also, the events are stretched horizontally, and they do not have any residual moveout.

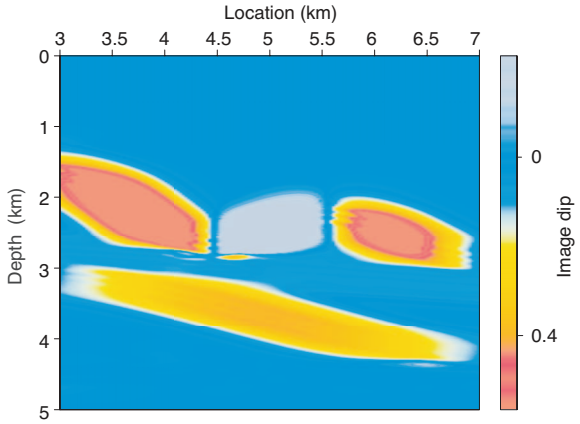


Figure 8. Local image-dip field for the second synthetic example.

Real data test

We use a portion of the 2D real data set from the Mahogany field in the Gulf of Mexico. The 2D data set is an ocean-bottom seismometer (OBS) multicomponent line that had been preprocessed by a seismic data-processing firm. The hydrophone (P) and vertical (Z) components of the geophone have been combined to form the PZ section, which represents the P-wave section. The data also have been separated into the PS section. We focus on both the PZ and the PS sections.

Figure 10 presents a typical shot gather. Figure 10a shows the PZ common-shot gather, and Figure 10b shows the PS common-shot gather. The PZ shot gather has fewer time samples than the PS shot gather because a longer time is needed to observe the converted-wave events. Also, note the polarity flip in the PS common-shot gather, a typical characteristic of this type of data.

In both data sets, the PZ and the PS sections were migrated using wave-equation shot-profile migration. Because the P and S velocity models are unknown for this problem, we migrate the data using a simple velocity model described by the function $v_{\text{mig}} = v_0 + gz_\xi$, where v_0, g, and z_ξ are the initial velocity, vertical gradient, and depth, respectively. For the PZ section, the values were $v_0 = 1500$ m/s and $g = 1.0\ \text{s}^{-1}$. For the PS section, the values were $v_0 = 800$ m/s and $g = 0.5\ \text{s}^{-1}$.

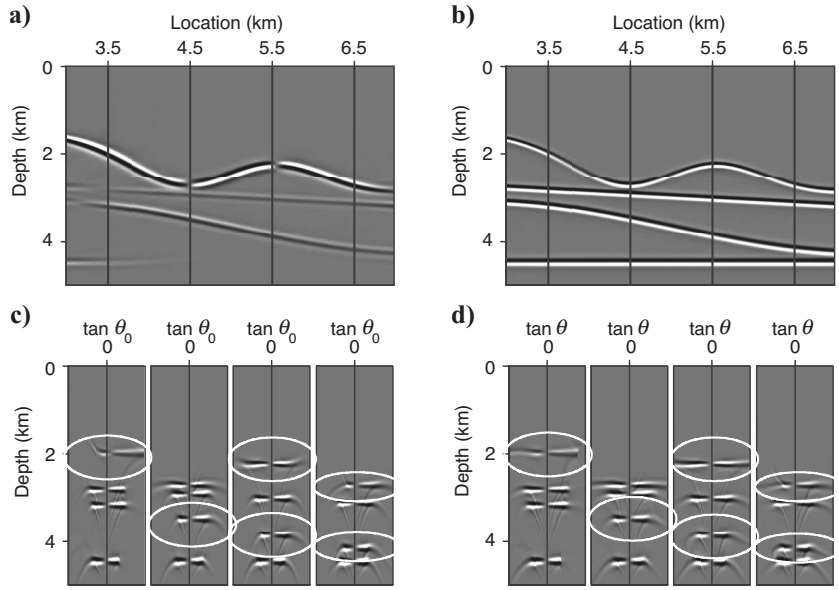


Figure 9. Final result for the second synthetic example. Views in the left column are the result for the PS section before correction. Views in the right column are the result for the PS section after correction. (a) The image at zero subsurface offset. (b) The image after stacking in the angle domain. (c) Four PS-ADCIGs. (d) The true PS-ADCIGs.

Figure 11 presents a PS image and two ADCIGs. Both CIGs are taken at the same location, indicated by the vertical line (location = 14,500 m) in the image. The PS image is taken at zero subsurface offset. This is not the ideal position because the polarity flip destroys the image at this location. The ideal case would be to flip the polarities in the angle domain. Unfortunately, we do not have the correct velocity model; therefore, we have only an approximate solution to the final PS image. However, through an update to the velocity model, we can obtain a more accurate image. The ADCIG in Figure 11b represents the ADCIGs obtained using the conventional methodology, which is tan θ_0 in Figure 2. The ADCIG in Figure 11c represents the proposed converted-wave ADCIG. Figure 12 represents the image-dip field for this experiment, which was estimated along the zero subsurface offset of the PS section.

The geology for this section consists of very gentle dips, representing a sedimentary depositional system with little structural deformation; therefore, the angle gather in Figure 11b has the polarity flip very close to zero angle. The proposed PS-ADCIG (Figure 11c) also preserves this characteristic. The residual curvature for the

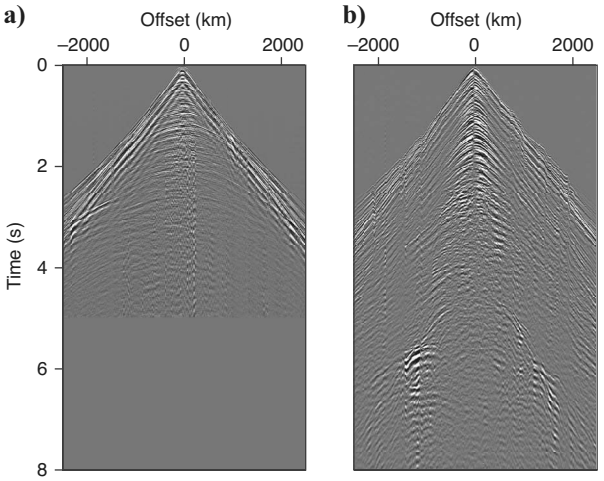


Figure 10. Typical common-shot gathers for the ocean-bottom seismic (OBS) Mahogany data set from the Gulf of Mexico. (a) Shot gather after PZ summation. (b) PS shot gather.

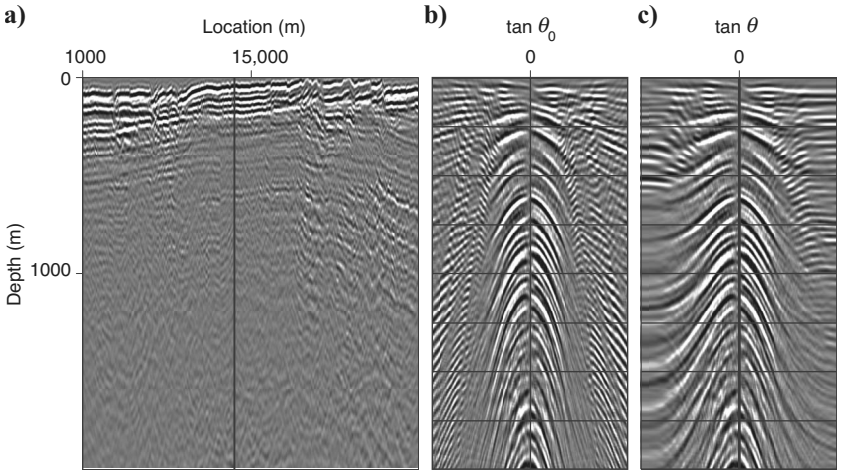


Figure 11. (a) PS image. (b, c) Two ADCIGs; both CIGs are taken at the same location, represented by the vertical line at CIG = 14,500 m in (a).

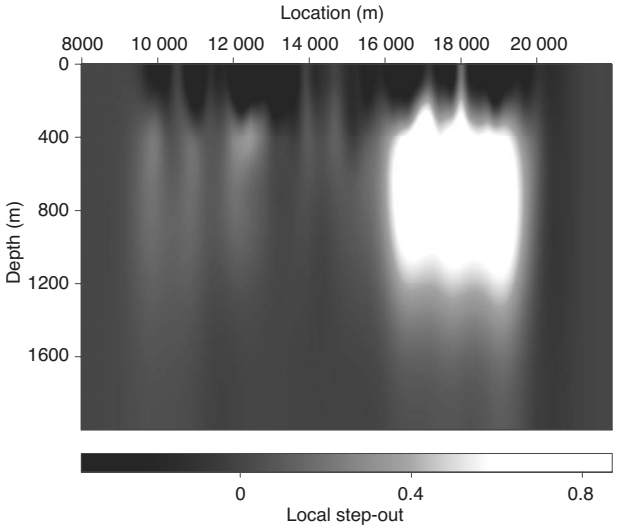


Figure 12. Image representing the field δ in equation 2.

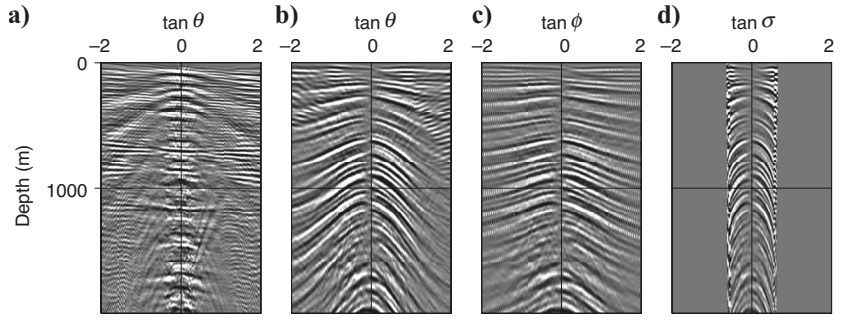


Figure 13. Compilation of angle-domain CIG for the 2D Mahogany data set; all of the CIGs are taken at the same image location (CIG = 14,500 m). (a) PZ-ADCIG. (b) PS-ADCIG. (c) P-ADCIG. (d) S-ADCIG.

events, whether primaries or multiples in Figure 11b, is larger than the residual curvature of the same events in the proposed PS-ADCIG.

Figure 13 compiles the ADCIGs for this data set, all of which are taken at the same position, location = 14,500 m. Shown are the PZ-ADCIG (Figure 13a), the proposed PS-ADCIG (Figure 13b), and both P- and S-angle-gather representations (Figure 13c and d) for the proposed PS-ADCIG. Notice that most of the primary events have a residual curvature. The residual moveout is more prominent for those events that we identify as multiples.

Notice that the angle coverage in both P- and S-ADCIG representations is smaller than for the true PS-ADCIG because the coverage of an individual plane wave is smaller than the combination of two plane waves, as is the case in converted-mode data.

The difference in the residual moveout between the single-mode PZ-ADCIG and the PS-ADCIG suggests an erroneous S-velocity model. Therefore, we ran a second migration for the PS section alone using a slower S-velocity model. The ratio between the first and second S-velocity models was two.

Figure 14 presents the PZ and updated PS results from using shot-profile migration. The PZ migration was done with the same P-velocity model as in the previous migration. The PS migration was done with the updated S-velocity model. Figure 14a, c, and e shows the PZ migration result; Figure 14a shows the image at zero subsurface-offset, and Figure 14c and e depicts four CIGs taken at locations indicated by the vertical lines in the zero subsurface image. Figure 14c represents SODCIGs, and Figure 14e represents ADCIGs. Most of the events in the ADCIGs are mainly flat, which suggests the initial linear P-velocity model is a reasonable approximation.

Figure 14b, d, and f shows the results of the PS migration. Figure 14b presents the stacking of the angle gathers after the polarity flip correction. Similar to the PZ results (14c), Figure 14d represents four SODCIGs. Figure 14f represents the true PS-ADCIGs that correspond to the SODCIGs at the locations indicated by the vertical lines in the angle-stack image. Note that most of the events in the PS-ADCIGs are approximately flat. Although there is a resemblance between the PZ and the PS images with respect to the general geology, the events do not match. There is a strong presence of multiples because of the shallow sea bottom (120 m). These multiples are more prominent in the PS section than in the PZ section because the PZ summation already eliminates the source ghost.

Finally, Figure 15 shows the same CIG as in Figure 13 but after the second migration for the PS section. This gather is taken at 14,500 m from the images in Figure 14. Figure 15a presents the PZ-ADCIG, Figure 15b presents the proposed PS-ADCIG, and Figure 15c and d is the PS-ADCIG representation in P-ADCIG and S-ADCIG, respectively. The events in all the different angle gathers are nearly flat, and several events in the PZ and PS angle gathers correlate. This suggests

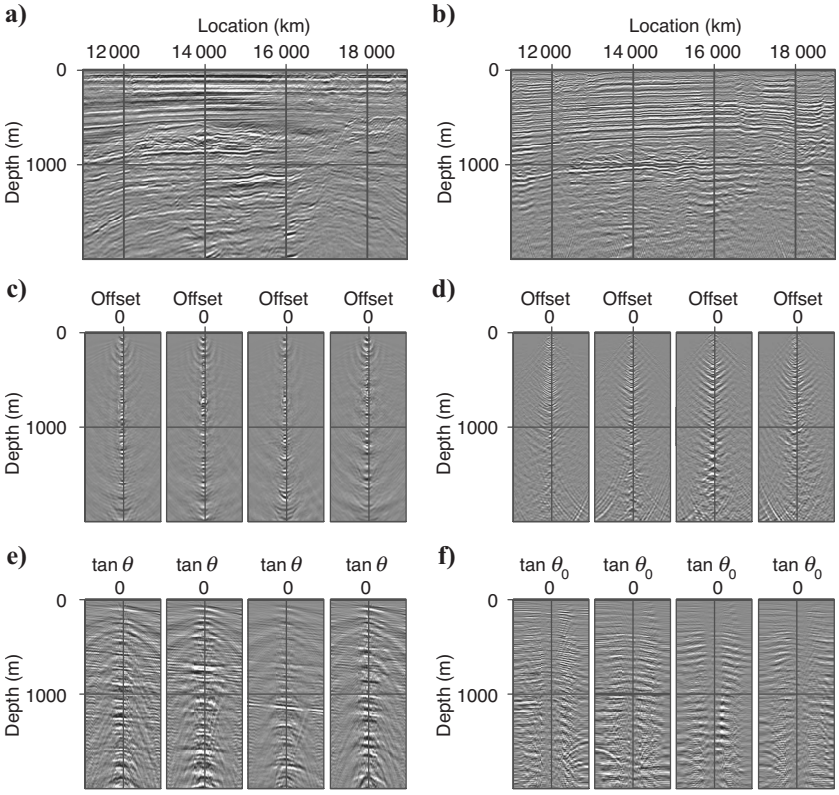


Figure 14. Final migration results. Views (a), (c), and (e) are the PZ result; views (b), (d), and (f) are the PS result. (a) Image at zero subsurface offset. (b) Angle stack after polarity flip correction. (c) Four SODCIGs taken at the marked locations in the image. (d) Four SODCIGs. (e) The ADCIGs. (f) True PS-ADCIGs.

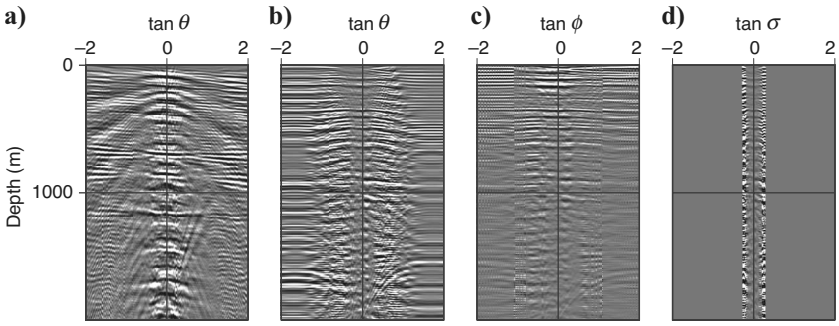


Figure 15. Compilation of ADCIG for the 2D Mahogany data set; all the CIGs are taken at the same image location (CIG = 14,500 m). (a) PZ-ADCIG. (b) PS-ADCIG. (c) P-ADCIG. (d) S-ADCIG.

that some of these reflections might come from the same geologic feature. Also note a residual moveout at high angles in the S-ADCIG for the first 1000 m. This information might be useful for a residual moveout analysis to compute an S-velocity perturbation, which might produce a final PS image that matches the PZ image for the main events.

CONCLUSIONS

The accurate transformation from SODCIGs into ADCIGs for the converted-mode case requires the information along the midpoint axis and the velocity ratio. Omitting this information leads to errors in the transformation that might result in incorrect velocity updates.

For the converted-mode case, the angle axis of the final image $I(m_\xi, \theta)$ after the transformation is neither the incidence nor the reflection angle but is the average of both. The half-aperture angle gathers can be transformed into two separate angle gathers, one representing the incidence angle and one representing the reflection angle. This transformation might yield useful information for the analysis of rock properties or velocity updates for the two different wavefields.

The next step will be to analyze how errors in either P or S velocity models are transformed in the PS-ADCIGs. This will result in both a formulation for the residual moveout of converted-mode data and a methodology for vertical velocity updates of both P and S velocity models.

ACKNOWLEDGMENTS

We would like to thank WesternGeco and CGG for providing the data set used in this paper. We also thank the sponsors of the Stanford Exploration Project for their support.

APPENDIX A

DERIVATION OF THE EQUATION FOR THE ANGLE-DOMAIN TRANSFORMATION

This appendix presents the derivation of the main equation for this paper, i.e., the transformation from the subsurface offset domain into the angle domain for converted-wave data.

The derivation follows the well-known equations for apparent slowness in a constant-velocity medium in the neighborhood of the reflection/conversion point. Our derivation is consistent with those presented by Fomel (2001); Sava and Fomel (2003); and Biondi (2007).

The expressions for the partial derivatives of the total traveltime with respect to the image point coordinates are as follows (Rosales and Rickett, 2001):

$$\frac{\partial t}{\partial m_\xi} = S_s \sin\beta_s + S_r \sin\beta_r,$$

$$\frac{\partial t}{\partial h_\xi} = -S_s \sin\beta_s + S_r \sin\beta_r,$$

$$-\frac{\partial t}{\partial z_\xi} = S_s \cos\beta_s + S_r \cos\beta_r, \qquad \text{(A-1)}$$

where S_s and S_r are the slowness (inverse of velocity) at the source and receiver locations. Figure A-1 illustrates all angles in this discussion. Angle β_s is the direction of the wave propagation for the

source, and angle β_r is the direction of the wave propagation for the receiver.

Through this set of equations, we obtain:

$$-\frac{\partial z_\xi}{\partial h_\xi} = \frac{S_r \sin\beta_r - S_s \sin\beta_s}{S_r \cos\beta_r + S_s \cos\beta_s},$$
$$-\frac{\partial z_\xi}{\partial m_\xi} = \frac{S_s \sin\beta_s + S_r \sin\beta_r}{S_s \cos\beta_s + S_r \cos\beta_r}. \quad \text{(A-2)}$$

We define two angles, α and γ, to relate β_s and β_r as follows:

$$\alpha = \frac{\beta_r + \beta_s}{2} \quad \text{and} \quad \theta = \frac{\beta_r - \beta_s}{2}. \quad \text{(A-3)}$$

Through the change of angles presented in equation A-3, and by following basic trigonometric identities, we can rewrite equations A-2 as follows:

$$-\frac{\partial z_\xi}{\partial h_\xi} = \frac{\tan\theta + \mathrm{S}\tan\alpha}{1 - \mathrm{S}\tan\alpha\tan\theta},$$
$$-\frac{\partial z_\xi}{\partial m_\xi} = \frac{\tan\alpha + \mathrm{S}\tan\theta}{1 - \mathrm{S}\tan\theta\tan\alpha}, \quad \text{(A-4)}$$

where

$$\mathrm{S} = \frac{S_r - S_s}{S_r + S_s} = \frac{\gamma(m_\xi, z_\xi) - 1}{\gamma(m_\xi, z_\xi) + 1}. \quad \text{(A-5)}$$

We introduce the following notation in equation A-4:

$$\tan\theta_0 = -\frac{\partial z_\xi}{\partial h_\xi},$$

$$\delta = -\frac{\partial z_\xi}{\partial m_\xi}.$$

In this notation, $\tan\theta_0$ represents the pseudoreflection angle and δ is the field for the local stepouts. The basis for this definition is in the conventional PP case, for which the pseudoreflection angle is the reflection angle and for which the field δ represents the geologic dip (Fomel, 2003). Based on this notation, equation A-4 can be rewritten as

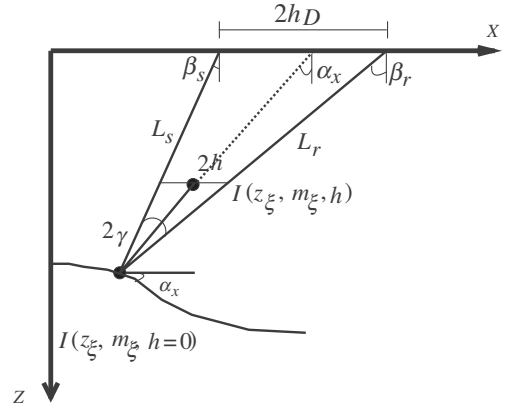


Figure A-1. Parametric formulation of the impulse response.

$$\tan\theta_0 = \frac{\tan\theta + \mathrm{S}\tan\alpha}{1 - \mathrm{S}\tan\alpha\tan\gamma}, \quad \text{(A-6)}$$

$$\delta = \frac{\tan\alpha + \mathrm{S}\tan\theta}{1 - \mathrm{S}\tan\theta\tan\alpha}. \quad \text{(A-7)}$$

Following basic algebra, equation A-7 can be rewritten as:

$$\tan\alpha = \frac{\delta - \mathrm{S}\tan\theta}{1 - \mathrm{S}\delta\tan\theta}. \quad \text{(A-8)}$$

Substituting equation A-8 into equation A-6 and following basic algebraic manipulations, we obtain equation 2 in the paper.

APPENDIX B

VALIDATION OF ANGLE-DOMAIN TRANSFORMATION THROUGH A KIRCHHOFF APPROACH

In this appendix, we obtain the relation to transform subsurface ODCIGs into ADCIGs for the case of PS data. To perform this derivation, we use the geometry in Figure A-1 to obtain the parametric equations for migration on a constant-velocity medium.

Following the derivation of Fomel (2003) and Sava and Fomel (2003) and applying simple trigonometry and geometry to Figure A-1, we obtain parametric equations for migrating an impulse recorded at time t_D, midpoint m_D, and surface offset h_D:

$$z_\xi = (L_s + L_r)\frac{\cos\beta_r \cos\beta_s}{\cos\beta_r + \cos\beta_s},$$
$$2h_\xi = 2h_D + (L_s + L_r)\frac{\sin\beta_s \cos\beta_r - \sin\beta_r \cos\beta_s}{\cos\beta_r + \cos\beta_s},$$
$$m_\xi = m_D - \frac{(L_s + L_r)}{2}\frac{\sin\beta_s \cos\beta_r + \sin\beta_r \cos\beta_s}{\cos\beta_r + \cos\beta_s}, \quad \text{(B-1)}$$

where the total path length is

$$t_D = S_s L_s + S_r L_r,$$
$$z_s - z_r = L_s \cos\beta_s - L_r \cos\beta_r. \quad \text{(B-2)}$$

From that system of equations, Biondi (2007) shows that the total path length is

$$L = \frac{t_D}{2}\frac{\cos\beta_r + \cos\beta_s}{S_s \cos\beta_r + S_r \cos\beta_s}. \quad \text{(B-3)}$$

We can rewrite system B-1 as:

$$z_\xi = \frac{(L_s + L_r)}{2}\frac{\cos^2\alpha - \sin^2\gamma}{\cos\alpha\cos\gamma},$$
$$2h_\xi = 2h_D - (L_s + L_r)\frac{\sin\gamma}{\cos\alpha},$$
$$m_\xi = m_D - \frac{(L_s + L_r)}{2}\frac{\sin\alpha}{\cos\gamma}. \quad \text{(B-4)}$$

where α and γ follow the same definition as in equation A-3. The value L in terms of the angles α and β is:

$$L(\alpha,\beta) = \frac{t_D}{(S_r + S_s) + (S_r - S_s)\tan\alpha\tan\gamma}. \quad \text{(B-5)}$$

Tangent to the impulse response

Following the demonstration done by Biondi (2007), the derivative of the depth with respect to the subsurface offset at a constant image point and the derivative of the depth with respect to the image point at a constant subsurface offset are given by

$$\left.\frac{\partial z_\xi}{\partial h_\xi}\right|_{m_\xi=\bar{m}_\xi} = -\frac{\left.\frac{\partial T}{\partial h_\xi}\right|_{m_\xi=\bar{m}_\xi}}{\left.\frac{\partial T}{\partial z_\xi}\right|_{m_\xi=\bar{m}_\xi}} = -\frac{\frac{\partial z_\xi}{\partial\alpha}\frac{\partial m_\xi}{\partial\gamma} - \frac{\partial z_\xi}{\partial\gamma}\frac{\partial m_\xi}{\partial\alpha}}{\frac{\partial m_\xi}{\partial\alpha}\frac{\partial h_\xi}{\partial\gamma} - \frac{\partial m_\xi}{\partial\gamma}\frac{\partial h_\xi}{\partial\alpha}}, \quad \text{(B-6)}$$

and

$$\left.\frac{\partial z_\xi}{\partial m_\xi}\right|_{h_\xi=\bar{h}_\xi} = -\frac{\left.\frac{\partial T}{\partial m_\xi}\right|_{h_\xi=\bar{h}_\xi}}{\left.\frac{\partial T}{\partial z_\xi}\right|_{h_\xi=\bar{h}_\xi}} = -\frac{\frac{\partial z_\xi}{\partial\gamma}\frac{\partial h_\xi}{\partial\alpha} - \frac{\partial z_\xi}{\partial\alpha}\frac{\partial h_\xi}{\partial\gamma}}{\frac{\partial m_\xi}{\partial\alpha}\frac{\partial h_\xi}{\partial\gamma} - \frac{\partial m_\xi}{\partial\gamma}\frac{\partial h_\xi}{\partial\alpha}}, \quad \text{(B-7)}$$

respectively, where the partial derivatives are

$$\frac{\partial z_\xi}{\partial\alpha} = -\frac{L}{\cos\alpha\cos\gamma}\left[\tan\alpha(\cos^2\alpha + \sin^2\gamma) + \frac{(S_r - S_s)\tan\gamma(\cos^2\alpha - \sin^2\gamma)}{\cos^2\alpha}\right],$$

$$\frac{\partial z_\xi}{\partial\gamma} = -\frac{L}{\cos\alpha\cos\gamma}\left[\tan\gamma(\cos^2\alpha + \sin^2\gamma) + \frac{(S_r - S_s)\tan\alpha(\cos^2\alpha - \sin^2\gamma)}{\cos^2\gamma}\right],$$

$$\frac{\partial m_\xi}{\partial\alpha} = -\frac{L}{\cos\gamma}\left[\cos\alpha - \frac{(S_r - S_s)\sin\alpha\tan\gamma}{\cos^2\alpha}\right],$$

$$\frac{\partial m_\xi}{\partial\gamma} = -\frac{L\sin\alpha}{\cos^2\gamma}\left[\sin\gamma - \frac{(S_r - S_s)\tan\alpha}{\cos\gamma}\right],$$

$$\frac{\partial h_\xi}{\partial\alpha} = -\frac{L\sin\gamma}{\cos^2\alpha}\left[\sin\alpha - \frac{(S_r - S_s)\tan\gamma}{\cos\alpha}\right],$$

and

$$\frac{\partial h_\xi}{\partial\gamma} = -\frac{L}{\cos\alpha}\left[\cos\gamma - \frac{(S_r - S_s)\tan\alpha\sin\gamma}{\cos^2\gamma}\right]. \quad \text{(B-8)}$$

Figure B-1 presents the analytical solutions for the tangent to the impulse response. This was done for an impulse at a PS traveltime of 2 s and a ϕ value of 2. Figure B-1a shows the solution for equation B-6. Figure B-1b shows the solution for equation B-7. The solid lines superimposed on both surfaces represent one section of the numerical derivative to the impulse response. The perfect correlation between the analytical and numerical solution validates our analytical formulations. This result supports the analysis presented with the kinematic equations (Appendix A).

APPENDIX C

ALTERNATIVE DERIVATION FOR THE ANGLE-DOMAIN TRANSFORMATION EQUATION

Sava and Fomel (2005) present an alternative derivation for transforming converted-wave ADCIGs. This appendix presents a summary for this deduction. We make the standard notations for the source and receiver coordinates: $s = m - h$, $r = m + h$. The traveltime from a source to a receiver is a function of all spatial coordinates of the seismic experiment, $t = t(m,h)$. Differentiating t with respect to m and h, and making the standard notations $\mathbf{p}_\alpha = \nabla_\alpha t$, where $\alpha = \{m,h,s,r\}$, we can write

$$\mathbf{p_m} = \mathbf{p_r} + \mathbf{p_s}, \quad \text{(C-1)}$$

$$\mathbf{p_h} = \mathbf{p_r} - \mathbf{p_s}. \quad \text{(C-2)}$$

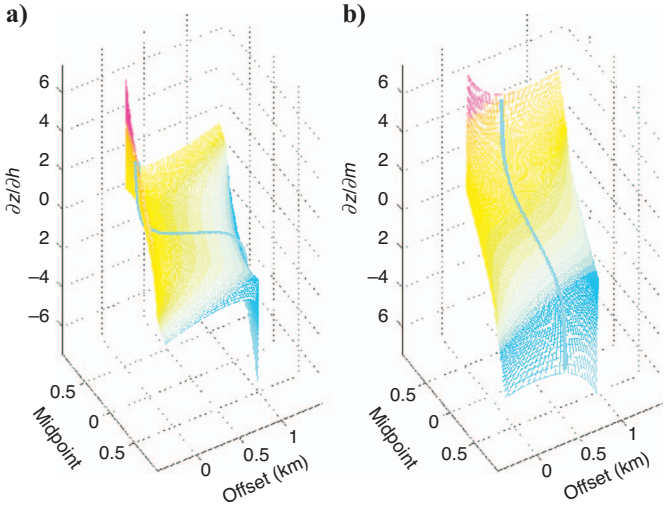


Figure B-1. Validation of the analytical solutions for the tangent to the impulse response. The surface represents the analytical solutions. Superimposed is the cut with the numerical derivative. (a) For equation C-6 and (b) for equation C-7, analytical solutions for the tangent of the spreading surface for different values of ϕ.

By definition, $|\mathbf{p_s}| = \mathbf{s_s}$ and $|\mathbf{p_r}| = \mathbf{s_r}$, where s_s and s_r are slownesses associated with the source and receiver rays, respectively.

For computational reasons, it is convenient to define the angles θ and δ using the following relations:

$$2\theta = \theta_s + \theta_r, \quad 2\delta = \theta_s - \theta_r. \tag{C-3}$$

Those two angles are the analogs of the image midpoint and offset coordinates. With them, we can find the reflection angles θ_s and θ_r by using the relations

$$\theta_s = \theta - \delta, \quad \theta_r = \theta + \delta. \tag{C-4}$$

Angle 2θ represents the opening between an incident ray and a reflected ray. Angle δ represents the deviation of the bisector of the angle 2θ from the normal to the reflector. For P-P reflections, $\delta = 0$.

Reflection angle θ

By analyzing the geometric relations of various $\mathbf{p}_\alpha$ vectors, we can write the following trigonometric expressions:

$$|\mathbf{p_h}|^2 = |\mathbf{p_s}|^2 + |\mathbf{p_r}|^2 - 2|\mathbf{p_s}||\mathbf{p_r}|\cos(2\theta), \tag{C-5}$$

$$|\mathbf{p_m}|^2 = |\mathbf{p_s}|^2 + |\mathbf{p_r}|^2 + 2|\mathbf{p_s}||\mathbf{p_r}|\cos(2\theta), \tag{C-6}$$

$$\mathbf{p_m} \cdot \mathbf{p_h} = |\mathbf{p_r}|^2 - |\mathbf{p_s}|^2. \tag{C-7}$$

We can transform this expression further using the notations $|\mathbf{p_s}| = \mathbf{s}$ and $|\mathbf{p_r}| = \gamma(m_\xi, z_\xi)s$, where $s(m_\xi, h_\xi)$ is the slowness associated with the incoming ray at every image point.

Solving for $\tan\theta$ from equations C-5 and C-6, we obtain an equivalent expression to equation 2 in the text for the reflection angle function of position and offset wavenumbers $(\mathbf{k_m}, \mathbf{k_h})$:

$$\tan^2\theta = \frac{[1 + \gamma(m_\xi, z_\xi)]^2|\mathbf{k_h}|^2 - [1 - \gamma(\mathbf{m}_\xi, \mathbf{z}_\xi)]^2|\mathbf{k_m}|^2}{[1 + \gamma(m_\xi, z_\xi)]^2|\mathbf{k_m}|^2 - [1 - \gamma(\mathbf{m}_\xi, \mathbf{z}_\xi)]^2|\mathbf{k_h}|^2}. \tag{C-8}$$

APPENDIX D

DERIVATION OF THE EQUATION FOR INDEPENDENT-ANGLE TRANSFORMATION

This appendix presents the derivation for the independent-angle transformation equations. The first element of this derivation is Snell's law:

$$\frac{\sin\phi}{v_p} = \frac{\sin\sigma}{v_s}. \tag{D-1}$$

From the definition of the full-aperture angle θ (equation 1), we obtain

$$\sigma = 2\theta - \phi, \tag{D-2}$$

$$\phi = 2\theta - \sigma. \tag{D-3}$$

Introducing equations D-2 and D-3 into equation D-1, and using the P-to-S velocity ratio γ, we obtain:

$$\sin\phi = \gamma\sin(2\theta - \phi), \tag{D-4}$$

$$\sin\sigma = \gamma^{-1}\sin(2\theta - \sigma). \tag{D-5}$$

Using simple trigonometric relations and basic algebra from equations D-4 and D-5, we get, respectively,

$$(1 + \gamma\cos 2\theta)\tan\phi = \gamma\sin 2\theta, \tag{D-6}$$

$$(\gamma + \cos 2\theta)\tan\sigma = \sin 2\theta. \tag{D-7}$$

Equations D-6 and D-7 translate into equations 3 and 4, respectively.

REFERENCES

Baina, R., P. Thierry, and H. Calandra, 2002, 3D preserved-amplitude prestack depth migration and amplitude versus angle relevance: The Leading Edge, **21**, 1237–1241.

Biondi, B., 2007, Angle-domain common-image gathers from anisotropic migration: Geophysics, **72**, no. 2, S81–S91.

Biondi, B., and W. W. Symes, 2004, Angle-domain common-image gathers for migration velocity analysis by wavefield-continuation imaging: Geophysics, **69**, 1283–1298.

Danbom, S. H., and S. N. Domenico, 1987, Shear-wave exploration: SEG.

de Bruin, C. G. M., C. P. A. Wapenaar, and A. J. Berkhout, 1990, Angle-dependent reflectivity by means of prestack migration: Geophysics, **55**, 1223–1234.

Fomel, S., 2001, Three-dimensional seismic data regularization: Ph.D. thesis, Stanford University.

———, 2002, Applications of plane-wave destruction filters: Geophysics, **67**, 1946–1960.

———, 2003, Velocity continuation and the anatomy of residual prestack time migration: Geophysics, **68**, 1650–1661.

———, 2004, Theory of 3-D angle gathers in wave-equation imaging: 74th Annual International Meeting, SEG, Expanded Abstracts, 1053–1056.

Prucha, M. L., B. L. Biondi, and W. W. Symes, 1999, Angle-domain common image gathers by wave-equation migration: 69th Annual International Meeting, SEG, Expanded Abstracts, 824–827.

Rickett, J., and P. Sava, 2002, Offset and angle-domain common image-point gathers for shot-profile migration: Geophysics, **67**, 883–889.

Rosales, D., and J. Rickett, 2001, PS-wave polarity reversal in angle domain common-image gathers: 71st Annual International Meeting, SEG, Expanded Abstracts, 1843–1846.

Sava, P. C., and S. Fomel, 2003, Angle-domain common-image gathers by wavefield continuation methods: Geophysics, **68**, 1065–1074.

———, 2005, Wave-equation common-angle gathers for converted waves: 75th Annual International Meeting, SEG, Expanded Abstracts, 947–950.

Stolk, C. C., and W. W. Symes, 2002, Artifacts in Kirchhoff common image gathers: 72nd Annual International Meeting, SEG, Expanded Abstracts, 1129–1132.

Zhang, Y., X. Sheng, N. Bleistein, and G. Zhang, 2007, True-amplitude, angle-domain, common-image gathers from one-way wave-equation migrations: Geophysics, **72**, no. 1, S49–S58.

Zhang, Y., G. Zhang, and N. Bleistein, 2003, Theory of true amplitude one-way wave equations and true amplitude common-shot migration: 73rd Annual International Meeting, SEG, Expanded Abstracts, 925–928.